JOURNAL OF GEOPHYSICAL RESEARCH, VOL. 114, C12008, doi:10.1029/2009JC005389, 2009

Wind stress in the presence of swell under moderate to strong wind conditions

H. García-Nava,[1] F. J. Ocampo-Torres,[1] P. Osuna,[1] and M. A. Donelan[2]

Received 18 March 2009; revised 6 July 2009; accepted 2 September 2009; published 8 December 2009.

[1] Wind stress is a key parameter for oceanic and atmospheric modeling, forecasting, and hydrodynamic studies. It is generally accepted that wind stress depends on the sea state. In particular, it has been shown that the presence of swell can modify both magnitude and direction of the wind stress. The presence of swell enhances momentum flux when swell propagates opposite to the wind direction and reduces it when it travels along the wind direction. However, those conclusions are mainly based on data acquired in low wind speed conditions and it is not clear to what extent an effect of swell persists at higher winds. Here simultaneous measurements of wind stress and waves, carried out in an area characterized by the occurrence of strong offshore winds with counter long-period swell, are presented and analyzed. The observations indicate that swell causes substantial changes to the wind stress at all observed wind conditions, including wind speeds as high as 20 ms^{-1}. It is believed that in low wind conditions swell increases drag by directly interacting with the air flow, whereas at higher winds, swell reduces drag by modifying the wind-sea-associated roughness.

Citation: García-Nava, H., F. J. Ocampo-Torres, P. Osuna, and M. A. Donelan (2009), Wind stress in the presence of swell under moderate to strong wind conditions, *J. Geophys. Res.*, *114*, C12008, doi:10.1029/2009JC005389.

1. Introduction

[2] Wind stress is relevant to a number of oceanic and atmospheric processes at different scales, including the global climate, large-scale atmospheric and oceanic circulations, storm development, wave generation, and mixed layer development. Thus, estimation of wind stress represents an issue of increasing importance for oceanic and atmospheric modeling, coupling and dynamic studies. Conventionally, wind stress τ is approximated using the mean wind speed at some fixed height over the ocean surface, usually 10 m, and a related drag coefficient C_D in the so called bulk aerodynamic formula

$$\tau = \rho C_D U_z^2, \tag{1}$$

where ρ is the air density and U_z is the wind speed at height z. C_D is a function of wind speed and measuring height itself, but it also depends on atmospheric stability and sea state. It follows from *Monin and Obukhov*'s [1954] similarity theory that, in neutrally stratified conditions, there is a unique relation between C_D and the surface roughness length z_0

$$C_{DN} = \kappa^2 [\log(z/z_0)]^{-2}, \tag{2}$$

where κ is the von Kármán constant and the subscript N denotes neutral conditions. In aerodynamically rough flows z_0 is expected to be related to the physical roughness of the sea surface, i.e., the waves. Consequently, it is common to discuss air-sea momentum transfer in terms of z_0 or C_D.

[3] Several studies have shown a dependence of the sea drag coefficient on the degree of development of the wind waves and have proposed parameterizations of z_0 in terms of wave age C_p/U_{10}, the ratio between wave phase velocity C_p and wind speed U_{10}; or alternatively C_p/u_*, where u_* is the friction velocity [e.g., *Donelan*, 1990; *Drennan et al.*, 2003]. Although these formulae seem to describe adequately the wind stress in pure wind sea conditions, it has been shown that the presence of swell obscures the relationship between roughness and wave age [*Drennan et al.*, 2005] reducing its applicability.

[4] In general, the presence of swell modifies the wind stress depending on wind speed and on swell properties [*Pan et al.*, 2005]. According to previous studies, the effect of swell also depends on the relative direction between wind and swell. When the swell propagates along the wind direction it tends to decrease the drag, if compared with open ocean estimates [*Drennan et al.*, 1999]. On the other hand, swell propagating across or against the wind direction produces an increase of drag [*Donelan et al.*, 1997; *Guo-Larsen et al.*, 2003]. These main experimental findings for the effect of swell on sea drag were reproduced qualitatively and quantitatively by *Kudryavstev and Makin* [2004] using a model that accounts for the impact of swell in the marine atmospheric boundary layer. In addition, it has been observed that the swell propagating at an angle to the wind direction causes deviations of the stress direction, and this

[1]Departamento de Oceanografía Física, Centro de Investigación Científica y de Educación Superior de Ensenada, Ensenada, Baja California, Mexico.

[2]Division of Applied Marine Physics, Rosenstiel School of Marine and Atmospheric Science, University of Miami, Miami, Florida, USA.

0148-0227/09/2009JC005389$09.00

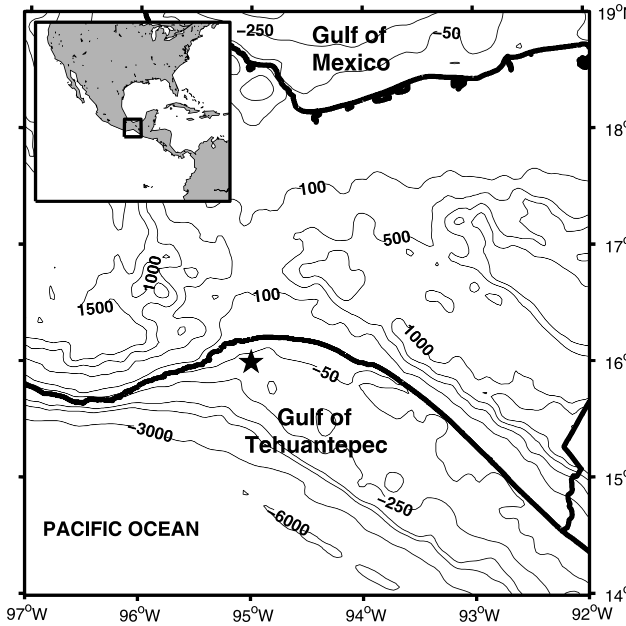

Figure 1. Location, bathymetry, and orography of the Gulf of Tehuantepec. The star represents the mooring site of the ASIS buoy.

deviation can be of such magnitude that the wind stress can oppose the mean air flow [*Geernaert et al.*, 1993; *Rieder et al.*, 1994; *Grachev et al.*, 2003]. However, these conclusions are based on data acquired during relatively low wind conditions with strong swell present and it is not yet clear to what extent swell effects persist at higher winds.

[5] The purpose of this work is to analyze the influence of swell on momentum flux in a large range of wind speeds. In particular, under the special conditions that occur when strong winds blow offshore, causing the coexistence of young wind seas and long-period counter swell.

[6] This paper is organized as follows: section 2 describes the study area and field campaign; data processing is outlined in section 3; in section 4 the general conditions observed during the field campaign are presented; and section 5 gives an analysis and discussion of the observed drag coefficient.

2. Gulf of Tehuantepec Experiment

2.1. Gulf of Tehuantepec

[7] The Gulf of Tehuantepec is a region located in the Mexican Pacific, between 93° and 96° W, and 15° and 16°30′ N. The Isthmus of Tehuantepec is the narrow region that separates the Gulf of Tehuantepec from the Gulf of Mexico (Figure 1).

[8] The Tehuantepec area is well known for the occurrence of strong offshore gap wind events called Tehuanos. A Tehuano occurs due to the conjunction of the following two phenomena: (1) the displacement of a high-pressure system, generated over the Great Plains of North America, toward the southern part of the Gulf of Mexico that causes a pressure difference between the Gulf of Mexico (high pressure) and the Gulf of Tehuantepec (low pressure); and (2) the existence of a mountain gap that accelerates the wind. The mountain range Sierra Madre del Sur, with a mean height of 2000 m above sea level, acts as a constraint to the air flow induced by the pressure difference between the Gulf of Mexico and the Gulf of Tehuantepec. In the central part of Isthmus of Tehuantepec the mean height drastically drops to 250 m forming a mountain gap of 40 km width, known as the Chivela Pass. As wind flow is constrained by the Sierra Madre it is driven into the Chivela Pass, which causes acceleration of the air flow. The result is the occurrence of strong wind events that reach the Gulf of Tehuantepec as offshore pulses.

[9] The Tehuano events are stronger and more common during winter. A single event can last from a few hours to several days, with mean wind speeds in excess of 20 ms^{-1}.

2.2. Air-Sea Interaction Experiment

[10] The Gulf of Tehuantepec air-sea interaction experiment (INTOA) took place from February to April 2005 in the Gulf of Tehuantepec, under the Study Programme for the Gulf of Tehuantepec (PEGoT, spanish acronym for Programa de Estudio del Golfo de Tehuantepec). The PEGoT is underway and aims for better knowledge of the strong and persistent offshore winds in the Gulf of Tehuantepec's coastal waters and their impact on the natural resources, as well as performing advance modeling of waves and surface current fields. As part of PEGoT one of the goals of INTOA was to improve our knowledge of air-sea interactions, with particular emphasis on the effects of surface waves on momentum flux in the peculiar local conditions that occur when the strong Tehuano winds blow offshore against a long-period Pacific swell.

[11] For INTOA an Air-Sea Interaction Spar (ASIS) buoy was moored from 22 February to 24 April 2005 in the central part of the Gulf of Tehuantepec at 16°N, 95°W, approximately 22 km offshore at a 60 m depth location (Figure 1). The ASIS buoy is a stable platform, especially designed for air-sea interaction studies, which causes very low distortion of surface and wind flow [*Graber et al.*, 2000]. Along with the mooring of the ASIS buoy INTOA included two HF Wellen Radar (WERA) stations, monitoring waves and surface currents in an 80 km diameter area; and three moored ADCP's, which provided information of coastal currents and waves. Here only data acquired from the ASIS buoy are considered. A more extensive description of INTOA will be given in a forthcoming paper by F. J. Ocampo-Torres et al. (manuscript in preparation, 2009).

3. Methods and Data

[12] For atmospheric turbulence measurements the ASIS was equipped with a sonic anemometer, which provided the three components of the wind velocity vector. Wave related parameters were measured using 8 capacitance wave staffs in a pentagonal array of 1 m diameter with 3 wave staffs placed near the center and one on each apex of the pentagon. Buoy motion was fully recorded using a three dimensional linear accelerometer, 3 orthogonal rate gyros, and a compass. Wind velocity, surface elevation, and buoy motion were sampled at 20 Hz. Additionally air temperature and humidity, atmospheric pressure, and water temperature were sampled at lower rates. All data were sampled continuously in 1 hour runs and stored on board. Details of the

Table 1. Sensors Used for Data Acquisition During INTOA[a]

Sensor	Manufacturer	Model	Sampling Frequency (Hz)	Height Above Sea Level (m)
Sonic anemometer	Gill	R3A	20	6.5
Wave staffs	Canadian Centre for Inland Waters		20	±1.25
Linear accelerometer	Columbia Research Laboratory	SA-307HPTX	20	−7
Rate gyros	Systron Donner Inertial Division	GC1-00050-100	20	−7
Compass	Precision Navigation Inc.	TCM-2	1	−7
Air temperature and humidity	Jautering Internatioal Corp.	MP101A	1	4.5
Barometer	Setra	270	1	4
Water temperature	Richard Brancker Research Ltd.	TR-1050P	0.2	−2.5

[a]The INTOA is a Gulf of Tehuantepec air-sea interaction experiment.

sensors used, as well as measuring heights, are given in Table 1.

[13] All data were processed in 30 minute blocks. Measured wind velocities and surface heights were corrected for buoy motion with a motion correction algorithm and the information from the motion sensors. Following *Anctil et al.* [1994], the velocity vector in an Earth-referenced coordinate system $\mathbf{U}_{true}$ is given by

$$\mathbf{U}_{true} = \mathbf{T}\mathbf{U}_{obs} + \boldsymbol{\Omega} \times \mathbf{T}\mathbf{L} + \mathbf{U}_{tras}, \tag{3}$$

where $\mathbf{U}_{obs}$ is the observed velocity, $\mathbf{U}_{tras}$ the buoy translation velocity, $\boldsymbol{\Omega}$ the angular buoy velocity, the vector $\mathbf{L} = [L_1, L_2, L_3]$ represents the distances of the motion sensors to the anemometer, $\mathbf{T}$ is the transformation matrix

$$\mathbf{T} = \begin{bmatrix} \cos\theta\cos\psi & \sin\theta\sin\phi\cos\psi - \cos\phi\sin\psi & \cos\phi\sin\theta\cos\psi + \sin\phi\sin\psi \\ \cos\theta\sin\psi & \sin\phi\sin\theta\sin\psi + \cos\phi\cos\psi & \cos\phi\sin\theta\sin\psi - \sin\phi\cos\psi \\ -\sin\theta & \sin\phi\cos\theta & \cos\phi\cos\theta, \end{bmatrix} \tag{4}$$

and θ, ϕ, and ψ are the x, y, and z axes rotation angles, respectively.

[14] The angular velocity $\boldsymbol{\Omega}$ was computed as the time derivative (upper dots) of the eulerian angles

$$\boldsymbol{\Omega} = \begin{bmatrix} -\dot{\theta}\sin\psi + \dot{\phi}\cos\theta\cos\psi \\ \dot{\theta}\cos\psi + \dot{\phi}\cos\theta\sin\psi \\ \dot{\psi} - \dot{\psi}\sin\theta \end{bmatrix} \tag{5}$$

and the translation velocity ($\mathbf{U}_{tras}$) by integration of the measured accelerations, $\mathbf{a} = [a_1, a_2, a_3]$, transformed to the Earth-referenced coordinate system,

$$\mathbf{U}_{tras} = \mathbf{T}\int \mathbf{a}dt. \tag{6}$$

[15] Using (6), equation (3) can by expressed as

$$\mathbf{U}_{true} = \mathbf{T}\mathbf{U}_{obs} + \boldsymbol{\Omega} \times \mathbf{T}\mathbf{L} + \mathbf{T}\int \mathbf{a}dt, \tag{7}$$

from which it can be shown that surface height in the Earth-referenced coordinate system $\mathbf{Z}_{true}$ is given by

$$\mathbf{Z}_{true} = \mathbf{T}\mathbf{Z}_{obs} + \int [\boldsymbol{\Omega} \times \mathbf{T}\mathbf{L}]dt + \mathbf{T}\iint \mathbf{a}dtdt. \tag{8}$$

Here $\mathbf{Z}_{obs}$ is the measured surface height, and the transformation matrix is reduced to $\mathbf{T} = [\cos\theta\cos\psi, \cos\theta\sin\psi, -\sin\theta]$ [*Drennan et al.*, 1994].

[16] According to *Monin and Obukhov* [1954] similarity theory, in a stationary and horizontally homogeneous atmospheric boundary layer, there exists a near surface layer where momentum fluxes are relatively height invariant. In this "constant stress layer," well above the thin viscous sublayer at the surface, momentum flux is carried by turbulent fluctuations

$$\boldsymbol{\tau} = -\rho\left[\overline{u'w'}\hat{\boldsymbol{i}}, \overline{v'w'}\hat{\boldsymbol{j}}\right], \tag{9}$$

where ρ is the air density, u' and v' are the horizontal along wind and across wind turbulent velocities, and w' is the vertical turbulent velocity. The overbar refers to a time average over a suitable interval.

[17] In order to compute wind stress from (9), corrected wind velocities were rotated into the mean wind direction. A mean tilt correction was applied to the wind velocities, to force $\overline{w} = 0$. The stress vector was calculated every 30 minutes after first detrending the data and assuming a constant density, ρ.

[18] Wind speeds were transformed to neutral values using the dimensionless wind speed profile parameter ψ_u from [*Donelan*, 1990]

$$U_{zN} = U_z + (u_*/\kappa)\psi_u(z/L), \tag{10}$$

where u_* is the friction velocity ($u_* = (|\boldsymbol{\tau}|/\rho)^{1/2}$), κ is the von Kármán constant ($\kappa \sim 0.41$), L is the Monin-Obukhov length scale

$$L = \frac{-u_*^3}{\kappa g\left(\overline{w'\xi'}/T_0 + 0.61\overline{w'q'}\right)}, \tag{11}$$

where T_0 is the reference absolute temperature, and ξ' and q' are the turbulent fluctuations of potential temperature and specific humidity, respectively. The terms $\overline{w'\xi'}$ and $\overline{w'q'}$ were computed from the heat H and moisture E fluxes calculated

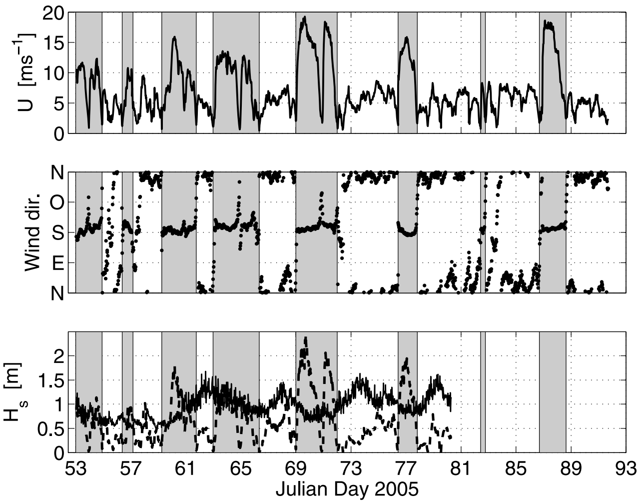

Figure 2. Time series of (top) mean wind speed, (middle) wind direction toward, and (bottom) significant wave height of swell (solid line) and wind sea (dashed line). The shaded areas denote the Tehuano events.

using bulk relations with constant Stanton C_H and Dalton C_E numbers of 0.0011 [*Smith*, 1989]

$$\overline{w'\xi'} = \frac{H}{\rho c_p} = -C_H(\Xi_z - \Xi_s)U_z, \tag{12a}$$

$$\overline{w'q'} = \frac{E}{\rho} = -C_E(Q_z - Q_s)U_z, \tag{12b}$$

where c_p is the specific heat at constant pressure and the subscript s denotes the surface values (Q_s is the saturated value of the specific humidity at the surface at temperature Ξ_s). As these bulk relations require neutral values as input, an iterative algorithm was used.

[19] Wind speed at the standard 10 m height was calculated assuming a logarithmic wind profile

$$U_{10N} = U_{zN} + \frac{u_*}{\kappa}\log\frac{10}{z}. \tag{13}$$

Subsequently, the neutral drag coefficient was computed from (1) and the surface roughness length from (2).

[20] Frequency spectra and mean wave parameters were obtained from the corrected surface elevation measurements. Significant wave height H_s was computed as $H_s = 4\sigma_\eta$, where σ_η is the standard deviation of the sea surface elevation, η. Directional wave spectra were calculated using the Maximum Likelihood Method (as described by *Drennan et al.* [1994]), when reliable information from at least four wave staffs was available.

[21] Since directional wave information is not available for the entire field campaign, partitioning of the wavefield into its swell and wind sea components was carried out based on frequency spectra $S(f)$. In order to separate $S(f)$ into wind sea and swell, a cut-off frequency f_c was setup as $f_c = 0.83g/2\pi U_{10}$ for fully developed wind seas [*Donelan et al.*, 1985], and $f_c = 0.7f_p$ for fetch limited wind seas, where $f_p = 13.7g\tilde{X}^{-0.27}/2\pi U_{10}$ is the peak frequency of fetch-limited wind seas [*Kahma and Calkoen*, 1996], and $\tilde{X} = gX/U_{10}^2$ is the dimensionless fetch. Frequencies higher than f_c were considered as wind sea and those below f_c as swell. The variance contained in each partition E_{part} was computed by integration of the frequency spectra over the corresponding frequency ranges. The significant wave heights for the partitions were computed as $H_s^{[part]} = 4E_{part}^{1/2}$.

4. Mean Conditions

[22] The conditions observed during INTOA are summarized in Figures 2 and 3. Within the analyzed period eight Tehuanos (shaded areas) were identified. The events lasted from less than 1 day to 3 days. During the Tehuanos the wind speed reached the maximum observed values, almost always exceeding 9 ms^{-1}, with overall maximum of 20 ms^{-1}. Wind directions were nearly constant toward south, and the atmospheric surface layer was close to neutral at the anemometer height except in those cases where a few hours relaxation of the wind speed occurred during the Tehuano (e.g., Julian days 65 and 71). In the periods between Tehuano events (inter-Tehuanos) winds were from south with some cases of southwesterlies. Wind speeds were below 9 ms^{-1}, and the atmospheric surface layer was predominantly stable.

[23] Air temperature ranged between 26° C and 33° C with a marked daily oscillation. Surface water temperature showed a less pronounced daily variation with values between 25° C and 29° C most of the time, except during Tehuano events when lower values were registered. The air was always warmer than the sea surface. The difference between air and subsurface temperature ranged from 2° C to 6° C, with the largest differences observed during the Tehuanos. Note, in Figure 3 the quick drop observed in the subsurface temperature when a Tehuano starts. Something similar occurs with the air relative humidity and, less noticeable, with the air temperature. This behavior is due to the presence of relatively colder and dryer air from the Gulf

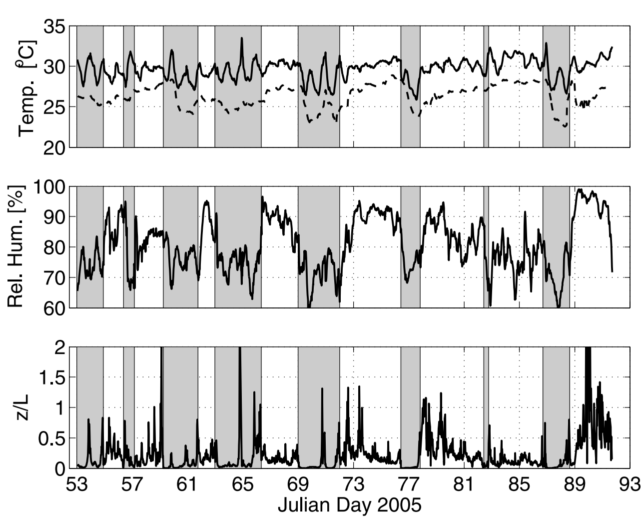

Figure 3. Time series of (top) air and subsurface temperature (solid and dashed lines, respectively), (middle) air relative humidity, (bottom) and atmospheric stability. The shaded areas denote the Tehuano events.

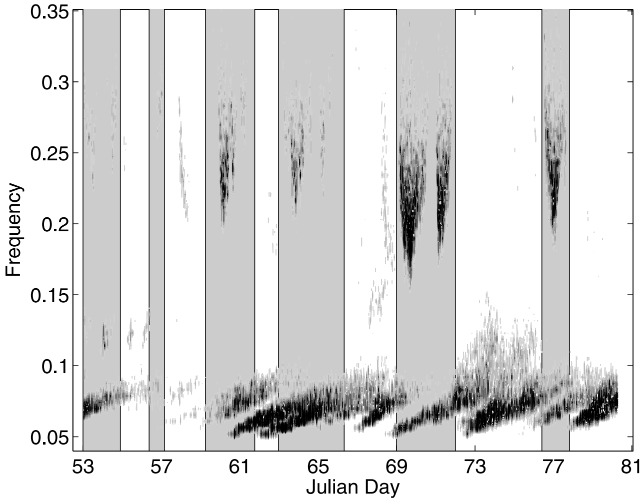

Figure 4. Spectral evolution of the wavefield. Grey scale represents spectral energy density. The shaded areas denote the Tehuano events.

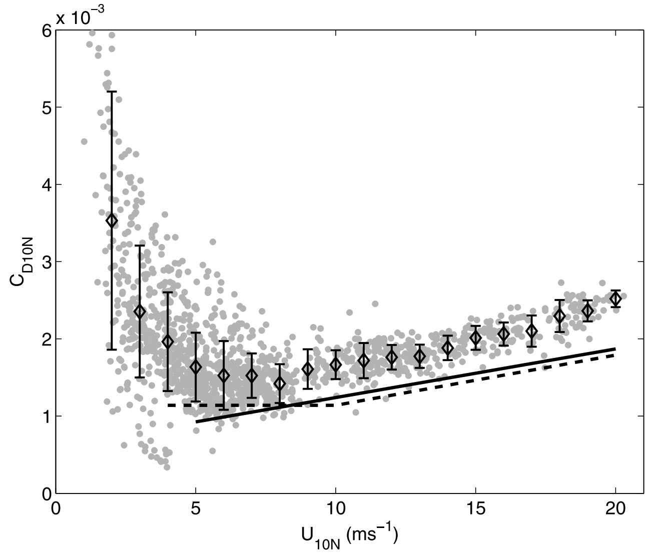

Figure 6. Observed drag coefficient versus neutral wind speed. Dots represent data values for each 30 minutes. Diamonds are the mean value of C_D for wind speed bins of 1 ms^{-1} and the error bars are 2 standard deviations. The lines are commonly used bulk formula from: *Smith* [1980] (solid line) and *Large and Pond* [1981] (dashed line).

of Mexico, and the entrainment of subsurface water into the surface caused by the enhanced mixing of the upper ocean layer [*Barton et al.*, 1993].

[24] The significant wave heights of wind sea and swell are shown in Figure 2 (bottom). It can be seen that the significant wave height of the swell at the ASIS buoy was between 0.5 and 1.4 m through the study period. Also, note that the highest wind waves occurred during the strongest Tehuano winds, and the highest significant height was 2.5 m at 20 ms^{-1} due to fetch limitation imposed by the coast. In Figure 4 the evolution of the frequency wave spectra is shown, the long-period swell that arrived to the area is clearly separated from the wind sea in the frequency domain. The presence of streak like patterns indicates that the arriving swell came from several storms. Longer waves travel faster than shorter ones, reaching the study area first. The slope of the streak patterns gives an idea of the distance to the storm (the place where all the waves were at the same time). Rough estimates give distances around 10,000 km, which suggests that swell came from storms somewhere in the Southern Pacific Ocean.

[25] The presence of swell results in swell running against winds during Tehuanos, and swell propagating along and across the wind direction during the inter-Tehuano periods. Typical directional spectra for both conditions are shown in Figure 5.

5. Drag Coefficient

[26] The neutral drag coefficient at 10 m height C_{D10N} is plotted versus wind speed U_{10N} in Figure 6. Dots represent

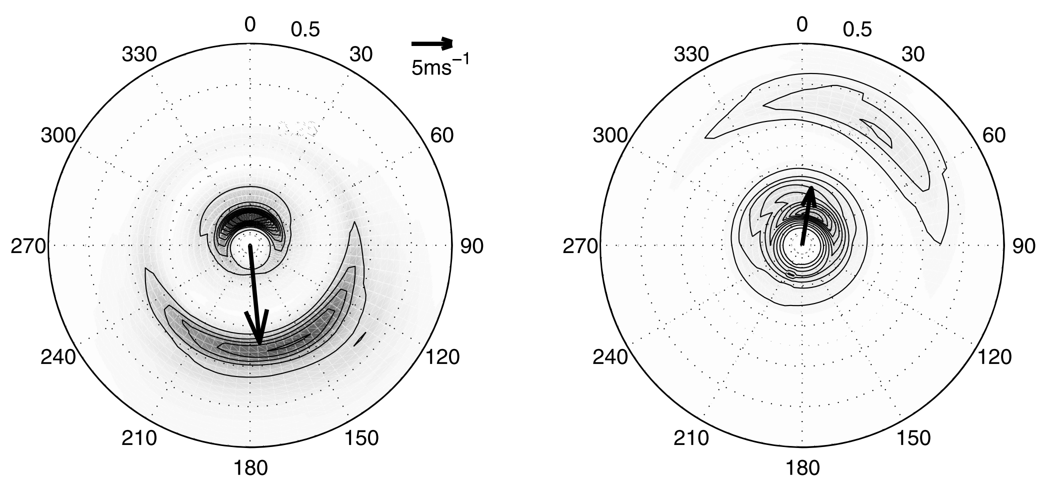

Figure 5. Typical directional wave spectra for (left) Tehuano events and for (right) inter-Tehuano events. Wind and wave directions are in the oceanographic convention. Contours represent energy density, dotted circles represent frequencies increasing in 0.1 Hz intervals, and arrows represent the horizontal mean wind vector.

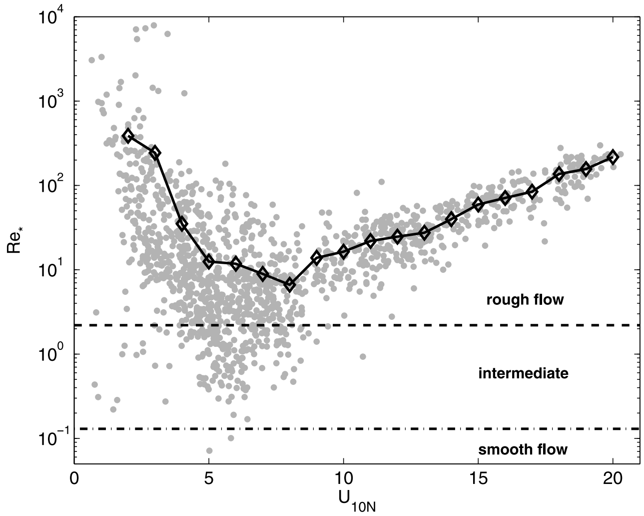

Figure 7. Roughness Reynolds number versus wind speed. Diamonds are the mean value for wind speed bins of 1 ms^{-1}. Lines represent the limits for rough (dashed line) and smooth (dash-dotted line) flow conditions.

data from each 30 minutes and error bars are one standard deviation of C_D in wind speed bins of 1 ms^{-1}. For visual purposes all data from the first bin (mean C_D = 9.7 × 10^{-3} ± 6.9 × 10^{-3}) and 4 data of the second bin were excluded from the graphic. In general terms, the observed C_D values are higher than those predicted from commonly used relationships. This is of particular importance for low wind conditions (4 ms^{-1} < U_{10} < 8 ms^{-1}), where computed values exceeded the constant value suggested by *Large and Pond* [1981]. In fact, C_D decreases as the wind increases from 0 to 8 ms^{-1}. At high wind conditions (U_{10} > 8 ms^{-1}) the observed drag coefficient exceeds from 20% to 50% the values computed using *Smith*'s [1980] and *Large and Pond*'s [1981] bulk relations (Figure 6).

5.1. Low Wind Conditions

[27] Previous field studies have suggested that the presence of swell modifies the drag at low winds. *Donelan et al.* [1997] observed an increase of the drag coefficient, up to 3 times, in light winds and counter swell conditions when compared with pure wind sea data. Furthermore, *Drennan et al.* [1999] observed a decreasing, and even negative values, of the drag coefficient in following swell conditions. These findings were confirmed by *Guo-Larsen et al.* [2003], who also found that cross swell increased the magnitude of the drag coefficient. *Kudryavstev and Makin* [2004] reproduced qualitatively and quantitatively the main experimental findings for the effect of swell on sea drag using a model that accounts for the impact of swell in the marine atmospheric boundary layer.

[28] A decrease of the drag coefficient with increasing wind speed was reported earlier by *Yelland and Taylor* [1996], from field observations in swell-dominated conditions on the Southern Ocean. More recently, *Pan et al.* [2005] confirmed that the decreasing drag coefficient is due to the presence of swell by comparing direct measurements obtained from the eddy correlation and the inertial dissipation methods. They found that the inertial dissipation method is unable to detect swell induced effects on the wind stress [cf. *Drennan et al.*, 1999]. They also proposed that the drag coefficient associated with swell is proportional to the swell steepness and inversely proportional to the ratio of the wind speed and the swell phase speed.

[29] The decrease of the drag coefficient with increasing wind speed at low wind conditions can be associated with other processes rather than solely with the presence of swell.

[30] As wind speed decreases the surface roughness decreases and a part of the stress begins to be supported by viscous forces. When the roughness elements are small enough not to protrude above the viscous sublayer the flow cannot feel them and becomes aerodynamically smooth [*Jones et al.*, 2001]. In an aerodynamically smooth flow the surface roughness length is given by

$$z_0 = 0.13\gamma/u_*, \tag{14}$$

where γ is the kinematic viscosity of the air. This implies that both the surface roughness length and the drag coefficient decrease with increasing wind speed. An aerodynamically smooth flow is characterized by a low roughness Reynolds number (Re_* = 0.13), whereas an aerodynamically rough flow is characterized by Re_* > 2.2. Roughness Reynolds number is defined by: $Re_* = z_0 u_*/\gamma$.

[31] As can be seen from Figure 7, the observed Re_* seldom reached smooth flow values although several cases with wind speeds between 5 and 7 ms^{-1} lay within the transitional flow range (0.13 < Re_* < 2.2). It is worth noticing that the lower value for Re_* will be expected to occur when $U \to 0$ as the viscous effects increase while the friction velocity and the roughness decrease. Nevertheless, *Wu* [1994] observed a minimum of Re_* at wind speeds around 5 ms^{-1} which he attributed to the increasing of the surface roughness caused by the presence of capillary waves. Here the occurrence of high values of Re_* at low wind speeds seems to reflect the effect of counter swell in acting as a roughness element and thus increasing the friction velocity.

[32] In Figure 8, it can be seen that the drag coefficient associated with a smooth flow, represented by the analytical solution for smooth flow blowing over a rigid wall (dashed line), decreases with increasing wind speed although the predicted values are much lower than the observations. In contrast, C_D from cases in the transitional flow range (triangles) are well represented by the *Smith* [1988] relationship (solid line), which considers that the surface roughness is the addition of the smooth and rough flow associated roughnesses.

[33] As $U \to 0$ the limit for forced convection is reached and the convection caused by buoyancy effects, free convection, becomes dominant. Free convection generates larger-scale structures than those typical of turbulence, usually with time scales of the order of 100 s [*Toba and Jones*, 2001]. These large structures can cause strong wind gusts that increase the drag coefficient at low winds, a phenomenon known as gustiness [*Drennan*, 2006].

[34] With the presence of structures with larger scales than the turbulence, the friction velocity becomes irrelevant as a velocity scale, and the convection velocity $w_* = (u_* F_B z_i)^{1/3}$ (where F_B is the buoyancy flux and z_i is

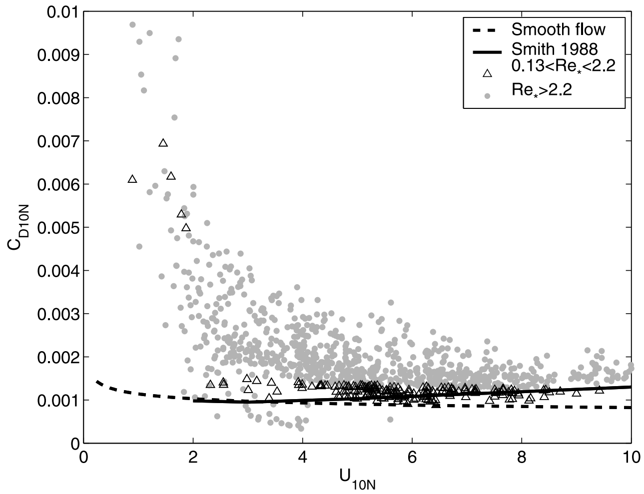

Figure 8. Drag coefficient versus wind speed for rough flow conditions (dots) and transitional flow conditions (triangles). Lines represent the C_D associated with a smooth flow (dashed line) and the *Smith* [1988] relationship (solid line).

the boundary layer thickness) is used instead. In order to include the effect of the wind gusts in the wind speed field, an effective velocity U_E is defined as $U_E = (U^2 + w_G^2)^{1/2}$, where $w_G = \beta w_*$ is the gust speed and β is a constant [*Godfery and Beljaars*, 1991]. According to *Grachev and Fairall* [1997] the effect of gustiness is important when the ratio $w_G/U > 0.5$. The values of w_G/U observed in this study were around 0.05, i.e., an order of magnitude below its critical value, which means that the high values of the drag coefficient observed at low winds are not related to gustiness, but rather to the presence of counter swell.

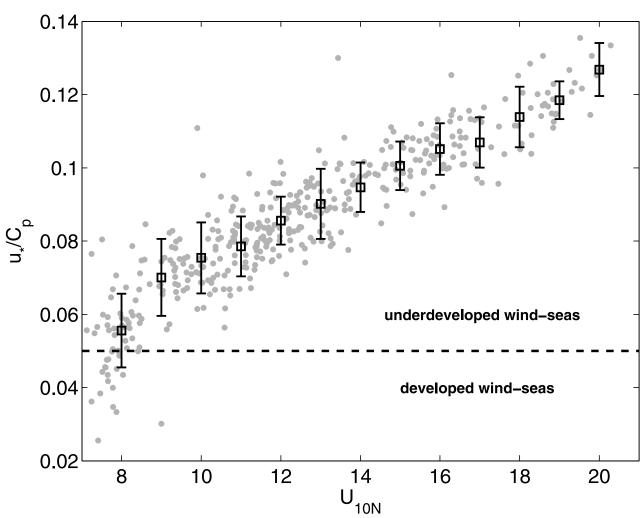

Figure 9. Inverse wave age (u_*/C_p) of wind generated waves versus neutral wind speed for high winds. Dots represent data values for each 30 minutes. Squares are mean wave age values for wind speed bins of 1 ms^{-1} and the error bars are 2 standard deviations. The dashed line represents the limit for fully developed wind seas.

5.2. Strong Wind Events

[35] During high wind conditions almost all data (94%) are for northerly winds. The northerly winds are offshore winds blowing over a fetch limited by the position of the ASIS buoy. Under these conditions the wind-generated waves were underdeveloped and became younger as the wind speed increased (Figure 9). Underdeveloped waves are expected to be rougher than their fully developed counterparts and therefore an increase of C_D is expected [*Drennan et al.*, 2003].

[36] In Figure 10 dimensionless roughness is plotted versus inverse wave age for fetch-limited cases (U > 7.5 ms^{-1} and $|\hat{\theta}| < 30°$, where $\hat{\theta}$ is the azimuthal wind direction). Although there is a slight tendency of roughness to decrease with increasing wave age, data are scattered and no clear relation can be noticed. This agrees with earlier reports that had pointed out that the presence of swell can mask the relationship between z_0 and C_p/u_* [*Donelan et al.*, 1993; *Drennan et al.*, 2005].

[37] In order to clarify the influence of swell on surface roughness, the effect of swell was reduced by selecting cases where the wind sea energy E_{ws} exceeded at least 5 times the swell energy E_s. This criterion is commonly used to define "pure wind sea" conditions [e.g., *Drennan et al.*, 2003, 2005]. However, the use of the term "wind-sea-dominated" conditions is preferred in this study, since the criterion $E_{ws} > 5E_s$ does not explicitly preclude the presence of swell. In fact, during wind-sea-dominated conditions the swell significant wave height ranged from 0.6 m to 1 m.

[38] For wind-sea-dominated conditions (solid dots in Figure 10) the expected increasing roughness for younger waves can be seen, but roughness values are smaller than those expected for pure wind sea conditions using the *Drennan et al.* [2003] relationship (dashed line in

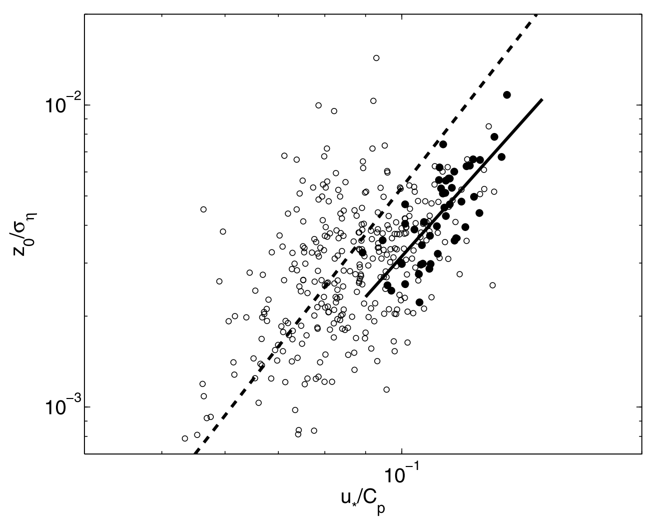

Figure 10. Dimensionless roughness versus inverse wave age for fetch-limited cases. Here σ_η is the standard deviation of surface elevation due to wind sea. Open dots represent data values for each 30 minutes. Solid dots are those data identified as wind sea dominated (see text for definition). Lines represent the logarithmic fit to wind-sea-dominated conditions (solid line) and the parameterization of *Drennan et al.* [2003] (dashed line).

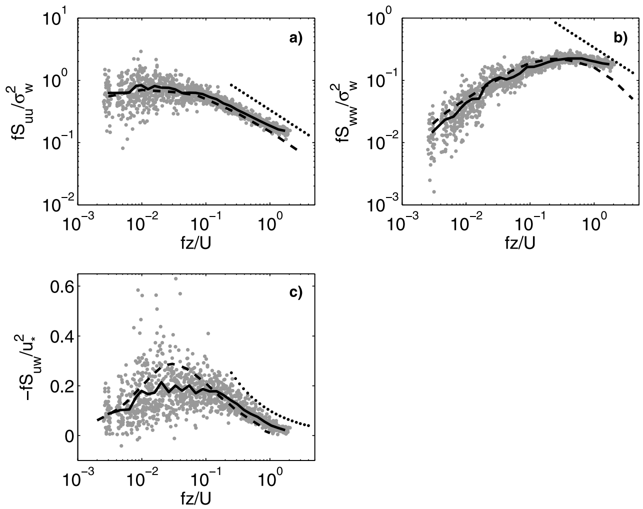

Figure 11. Spectra of (a) u, (b) w, and (c) cospectrum uw for wind-sea-dominated conditions plotted in the universal scaling of *Miyake et al.* [1970]. Lines represent the mean value for wind-sea-dominated conditions (solid line), the universal spectral shape of *Miyake et al.* [1970] (dashed line), and the inertial subrange slope (dotted line).

Figure 10). It should be noticed that spurious correlation might affect the relation between dimensionless roughness and wave age since both quantities depend on u_*. Nonetheless, some evidence of a reduction of stress under these conditions will be shown next.

[39] From Monin Obukhov similarity theory, it is expected that wind velocity spectra will follow a universal shape when properly scaled. *Miyake et al.* [1970] demonstrated this universality over the ocean using the standard deviation of the vertical velocity σ_w as the scaling variable for the velocity spectra and the friction velocity for the uw cospectrum. More recently, *Drennan et al.* [1999] confirmed these findings for fetch-limited pure wind sea conditions and found a substantial departure from the universal curves in light winds with fast swell running in the same direction.

[40] In Figure 11 the u and w spectra (Figures 11a and 11b, respectively), and uw cospectrum (Figure 11c) of the wind-sea-dominated conditions are plotted using *Miyake et al.*'s [1970] scaling. For visual purposes each spectrum has been averaged using equally spaced logarithmic bins. In general, there is good agreement with the universal spectral shape of *Miyake et al.* [1970] (dashed line) for the u and w spectra. In the inertial subrange however, values are higher than those predicted by the universal shape. Regarding the uw cospectrum, the results show significant departure from the universal curve at frequencies below the inertial subrange, especially at the swell and lower frequencies, where the momentum transfer is greatly reduced or even upward. Although there is some more scatter from each single run the same mean features can be seen for the whole fetch-limited data set.

[41] The presence of swell can modify the drag in at least the following two different ways: (1) by exchanging momentum with the wind field and (2) by altering the wind sea part of the spectrum, which leads to a change in the aerodynamic roughness of the sea surface. It has been noticed that the presence of swell in the form of paddle-generated waves can induce a reduction of the energy level of the wind-generated waves in tank experiments [e.g., *Phillips and Banner*, 1974; *Donelan*, 1987; *Makin et al.*, 2007], hence reducing the wind sea associated roughness. In opposing winds the direct contribution of swell to the drag is expected to be very large and to compensate for any reduction in the wind sea supported part of the drag [*Donelan and Dobson*, 2001]. However, the significance of the direct contribution of swell to drag decreases dramatically with increasing wind speed [*Pan et al.*, 2005]. Thus, for high wind the reduction of drag due to modification of the wind sea can overwhelm the direct swell contribution, and hence the overall effect will be a reduction in C_D.

[42] In Figure 12 the observed dimensionless energy $\epsilon_* = g^2E/u_*^4$ and H_s for wind seas during fetch-limited conditions are compared with those predicted from *Kahma and Calkoen*'s [1996] expression for the same conditions in the absence of swell. Figure 12a shows observed ϵ_* versus dimensionless fetch $\chi_* = gX/u_*^2$, lines are the linear fit (solid) and *Kahma and Calkoen*'s [1996] expression (dotted). It can be seen that observed energy values are lower than those expected in the absence of swell for the whole range of χ_*. Figure 12b shows the comparison between observed wind sea H_s and computed H_s using *Kahma and Calkoen*'s [1996] relationship (dotted line in Figure 12a). It is easily noticed that observed H_s are consistently lower than those predicted. These results must be taken with caution since different results might be expected when using the different data sets available from the work of *Kahma and Calkoen* [1996]. Here the composite data set was used [cf. *Romero and Melville*, 2009] because it fits better the overall conditions observed during the Tehuano events (H. García-Nava et al., manuscript in preparation, 2009).

[43] We now compare the observed drag coefficient, hereinafter C_{Dobs}, with that expected in the absence of swell, C_{Dpws}. The expected roughness length for underdeveloped pure wind seas was computed from wind sea

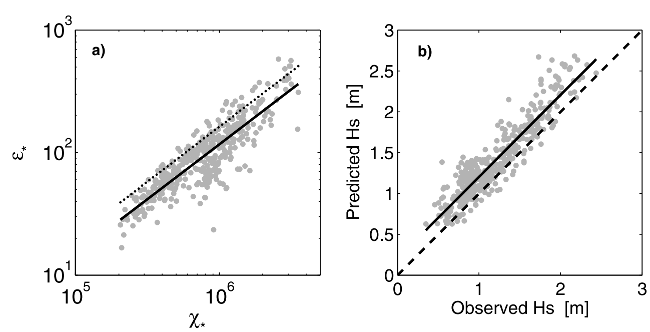

Figure 12. Comparison between observed fetch-limited wind sea properties and those predicted from *Kahma and Calkoen*'s [1996] expression. (a) Observed dimensionless wind sea energy versus dimensionless fetch; lines represent the linear fit (solid line) and *Kahma and Calkoen*'s [1996] expression (dotted line). (b) Observed wind sea H_s versus predicted wind sea H_s; lines are the linear fit (solid line) and equality line (dashed line).

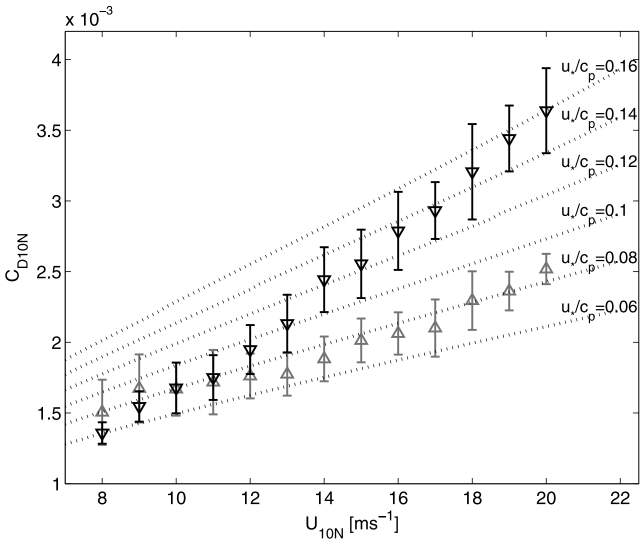

Figure 13. Drag coefficient versus neutral wind speed for data identified as fetch limited. Triangles and inverse triangles are the mean values, in wind speed bins of 1 ms^{-1}, of observed and computed pure wind sea C_D, respectively. Dotted lines represent the expected C_D for particular constant values of wave age under fetch-limited pure wind sea conditions, according to *Drennan et al.* [2003].

observed parameters, using the *Drennan et al.* [2003] relationship. Then, C_{Dpws} was obtained from (2).

[44] In Figure 13 it can be seen that for winds higher than 12 ms^{-1} C_{Dpws} (down triangles) are higher than C_{Dobs} (up triangles) and that the difference increases with increasing wind speed. For winds speeds between 10 ms^{-1} and 12 ms^{-1} C_{Dobs} and C_{Dpws} are similar, while observed values seem to be higher for winds lower than 10 ms^{-1}. In general, observed drag coefficients are best described with a constant wave age around 0.08. This corresponds to a Charnock constant α of 0.023 which is 24% larger than the commonly used value of 0.0185.

[45] The results shown in Figure 13 suggest that the reduction of wind sea roughness caused by the presence of counter swell exceeds the enhancement for winds higher than 12 ms^{-1}, while for lower winds the direct contribution of swell to drag balances the reduction, and no clear effect of swell can be noticed. This conclusion is supported by Figure 14, where dimensionless roughness is plotted against inverse wave age for data in 1 ms^{-1} wind speed bins. Figure 14 also shows that, for winds below 10 ms^{-1}, observed wind sea roughness tends to be higher than expected for pure wind sea conditions. Also, notice that the mean values for winds greater than 13 ms^{-1} resemble the regression line drawn for wind-sea-dominated cases in Figure 10.

[46] Several mechanisms have been proposed for the observed suppression of wind waves by longer waves. When the wind blows over the water it induces a very thin layer of highly sheared current near the surface. This current is known as wind drift. *Phillips and Banner* [1974] suggested that long waves moving across the surface increase the wind drift near the crest of the long waves and this increase can be of such magnitude that the maximum particle speed of the wind generated waves (shorter waves) exceeds their phase speeds causing enhanced wave breaking. However, *Wright* [1976] found that this hypothesis overpredicts the attenuation of wind waves and that the wind dependence of the attenuation appears to be contrary to that predicted, leading to nearly no suppression at higher winds. *Masson* [1993] showed that the nonlinear coupling, due to resonant interaction, between swell and wind sea produces an energy flux that smooths out the high-frequency peak. However, she also found that the coupling is generally negligible unless the two peaks are very close to each other. More recently, *Chen and Belcher* [2000] suggested that the suppression of wind waves by a longer wave is due to the direct coupling between the long wave and the wind. They developed a model in which they supposed that long waves absorb momentum from the wind reducing the turbulent momentum flux available in the wind to generate waves, and showed that the reduction of the energy density of wind waves depends directly on the swell steepness and inversely on the ratio C_p/u_*, where C_p is the phase speed of the swell. Since ocean swell characteristically corresponds to fast and smooth waves they conclude that this effect is very small in the ocean.

[47] It seems that none of the above mentioned mechanisms explains the attenuation of wind sea roughness suggested here. The observed swell is characterized by low steepness, $ak \sim 0.02$, and the ratio $C_{p_{swell}}/u_*$ varies from 20 at the highest wind speeds to 70 at moderate winds. According to the results of *Chen and Belcher* [2000] these swell properties will lead to very low reduction of the wind sea amplitude. Furthermore, the *Chen and Belcher* [2000] hypothesis assumes that swell absorbs momentum from the wind and, since observed conditions correspond to swell opposing winds, it is expected that the direct coupling of swell and wind results in releasing of momentum from swell to the wind rather than an uptake [see *Donelan et al.*, 1997]. The observed swell and wind sea spectral peaks are far apart in frequency space (Figure 4), so that energy flux by

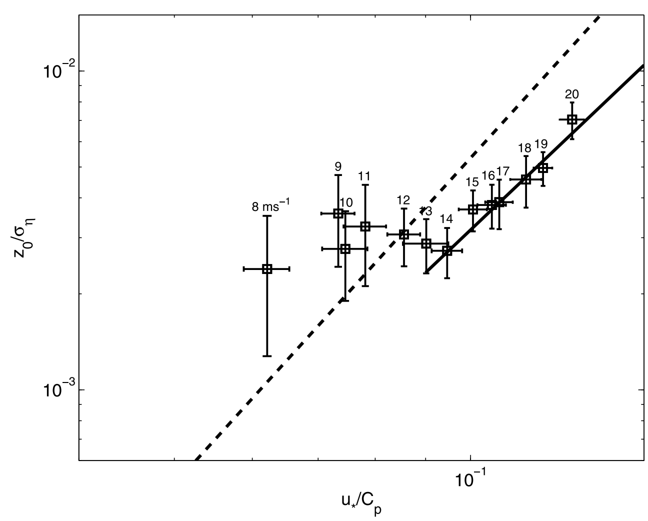

Figure 14. Same as in Figure 10 but data are averaged in wind speed bins of 1 ms^{-1} (squares). Error bars are 1 standard deviation. Numbers are the mean wind speed for each bin.

nonlinear coupling, if it exists, should be negligible [*Masson*, 1993].

6. Conclusions

[48] An ASIS buoy was successfully deployed in the Gulf of Tehuantepec, Mexico, in order to record air-sea interaction variables in a large range of wind speeds and sea states. Acquired data suggest that the presence of swell causes substantial changes in the wind stress for all wind conditions observed.

[49] Under low winds the observed C_D decreases with wind speed and its values exceed by a factor of 2 or more the values computed from commonly used relationships. It is believed that under these conditions the direct interaction between counter swell and the air flow increases the drag, causing enhanced C_D with a large variability.

[50] In moderate to high wind conditions, the observed stress is lower than the expected for underdeveloped rough pure wind seas. As an hypothesis, we suggest that the presence of counterswell reduces the associated wind sea roughness and hence causes a reduction of C_D. This reduction of C_D is directly wind dependent and, around wind speeds of 10–12 ms^{-1}, is compensated by an increase of drag caused by direct interaction of the swell with the wind. These results correspond to underdeveloped wind seas interacting with strong opposing swell. These conditions are expected to occur in coastal areas subjected to moderate to strong offshore winds. However, it is possible that swell causes a similar indirect reduction of C_D through wind sea roughness modification in fully developed seas [see *Young*, 2006].

[51] A constant Charnock parameter $\alpha = 0.023$ describes reasonably well the high wind C_D data, but a proper parameterization of the reduction of wind sea roughness caused by swell is needed in order to improve drag estimates over the ocean.

Appendix A: Error Analysis

[52] The potential errors of correcting wind data by buoy motion can be determined using standard error analysis techniques. The uncertainty of a given function $q(x_1, x_2, .., x_n)$ can be expressed as [*Taylor*, 1997]

$$\delta q \approx \left|\frac{\partial q}{\partial x_1}\right|\delta x_1 + \left|\frac{\partial q}{\partial x_2}\right|\delta x_2 + .. + \left|\frac{\partial q}{\partial x_n}\right|\delta x_n, \qquad \text{(A1)}$$

where δx_i represents the uncertainty of variable x_i. If δx_1, δx_2, .., δx_n are independent and random, the uncertainty of q, $\delta\, q$, becomes

$$\delta q = \left[\left(\frac{\partial q}{\partial x_1}\delta x_1\right)^2 + \left(\frac{\partial q}{\partial x_2}\delta x_2\right)^2 + .. + \left(\frac{\partial q}{\partial x_n}\delta x_n\right)^2\right]^{1/2}. \qquad \text{(A2)}$$

[53] The wind speed error induced by motion correction can be computed by applying (A2) to (3), then

$$\delta \mathbf{U}_{true} = \left[(\beta_\theta \delta\theta)^2 + (\beta_\phi \delta\phi)^2 + (\beta_\psi \delta\psi)^2 + (\beta_{u_a} \delta \mathbf{U}_{tras})^2\right]^{1/2}, \qquad \text{(A3)}$$

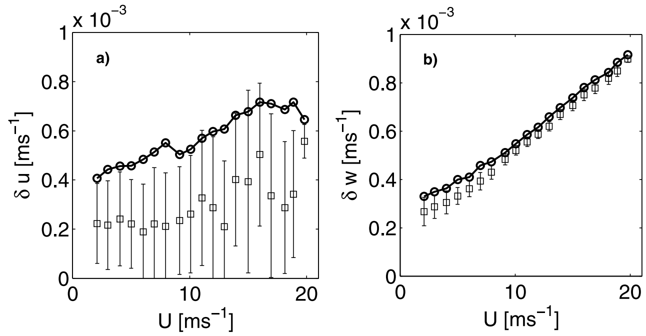

Figure A1. Motion correction induced errors for (a) u and (b) w versus wind speed. The squares and the error bars represent the mean value and the 99% confidence limits for wind speed bins of 1 ms^{-1}, respectively. Circles are the maximum observed value for each wind speed bin.

where β_θ, β_ϕ, β_ψ, and β_{u_a} are given by

$$\begin{aligned}
\beta_\theta &= \frac{\partial \mathbf{T}}{\partial \theta}\mathbf{U}_{obs} + \frac{\partial \boldsymbol{\Omega}}{\partial \theta} \times \mathbf{TL} + \boldsymbol{\Omega} \times \frac{\partial \mathbf{T}}{\partial \theta}\mathbf{L} + \frac{\partial \mathbf{T}}{\partial \theta}\mathbf{U}_{tras},\\
\beta_\phi &= \frac{\partial \mathbf{T}}{\partial \phi}\mathbf{U}_{obs} + \frac{\partial \boldsymbol{\Omega}}{\partial \phi} \times \mathbf{TL} + \boldsymbol{\Omega} \times \frac{\partial \mathbf{T}}{\partial \phi}\mathbf{L} + \frac{\partial \mathbf{T}}{\partial \phi}\mathbf{U}_{tras},\\
\beta_\psi &= \frac{\partial \mathbf{T}}{\partial \psi}\mathbf{U}_{obs} + \frac{\partial \boldsymbol{\Omega}}{\partial \psi} \times \mathbf{TL} + \boldsymbol{\Omega} \times \frac{\partial \mathbf{T}}{\partial \psi}\mathbf{L} + \frac{\partial \mathbf{T}}{\partial \psi}\mathbf{U}_{tras},\\
\beta_{u_a} &= \mathbf{T}.
\end{aligned} \qquad \text{(A4)}$$

The motion correction induced errors for u and w, computed from (A3), are plotted in Figure A1 as a function of wind speed. The error bars represent the 99% confidence limits for wind speed bins of 1 ms^{-1} and the circles the maximum observed value for each wind speed bin. It can be seen that both δu and δw increase with increasing wind speed. Remarkably δw presents a clear trend and reduced scatter, maybe caused by its great dependence on wind-sea-induced motion. The maximum motion correction induced errors are $|\delta u|_{\max} < 0.7 \times 10^{-3}$ and $|\delta w|_{\max} < 0.9 \times 10^{-3}$, for $\delta\, u$ and δw, respectively.

[54] Including δu and δw errors in the wind stress computation leads to

$$\begin{aligned}
-\tau/\rho &= \overline{(u-U)(w-W)}\\
&= \overline{(u'+\delta u)(w'+\delta w)}\\
&= \overline{u'w'} + \overline{u'\delta w} + \overline{w'\delta u} + \overline{\delta u \delta w},
\end{aligned} \qquad \text{(A5)}$$

where u' and w' represent the total wind speed fluctuations, i.e., shear induced and wave coherent fluctuations [cf. *Pan et al.* 2005]. By comparing equations (9) and (A5) it can be shown that the motion correction induced error on wind stress ($\delta\overline{uw}$) is given by

$$\delta\overline{uw} = \overline{u'\delta w} + \overline{w'\delta u} + \overline{\delta u \delta w}. \qquad \text{(A6)}$$

Alternatively, a more conservative computation can be obtained by approaching $\delta\overline{uw}$ as [*Pan et al.*, 2005]

$$\delta\overline{uw} \le \overline{|u'|}|\delta w|_{\max} + \overline{|w'|}|\delta u|_{\max} + |\delta u|_{\max}|\delta w|_{\max}. \qquad \text{(A7)}$$

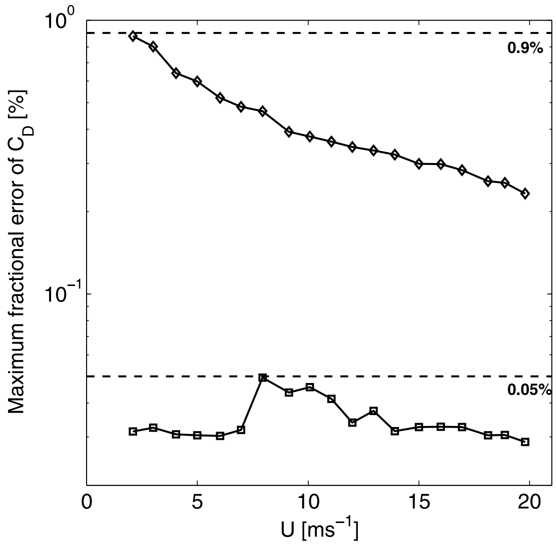

Figure A2. Fractional error of C_D induced by motion correction versus wind speed. Computed with two different methods: direct (squares) and conservative (diamonds); see text for definition.

[55] Propagation of $\delta\overline{uw}$ through C_D calculation yields

$$\delta C_D = \frac{\delta\overline{uw}}{U^2}, \tag{A8}$$

where δC_D is the error on drag coefficient due to motion correction, and the fractional error induced on mean wind speed was neglected $\delta u/|U| \sim 0$.

[56] Here δC_D was computed in two different ways, named: direct, computing δC_D from equations (A6 and A8); and conservative, by first computing $\delta\ \overline{uw}$ from equation (A7) using the maximum values of δu and δw for wind speed bins of 1 ms^{-1} (circles in Figure A1), and combining this result with equation (A8).

[57] The maximum fractional error of C_D induced by motion correction is less than 0.05% for δC_D computed directly (squares in Figure A2) and at most 0.9% if computed with the conservative method (circles in Figure A2). In any case, the motion induced error on C_D is negligible.

[58] **Acknowledgments.** We thank all the people who contributed to the success of this work, i.e., Mike Rebozo, Neil Williams, Joe Gabriele, and Sergio Ramos, as well as the officers and crew of the DR06 ARM *Bahía Tepoca*, and the members of CICESE's Waves Group GOL. Especial thanks to W. Drennan for his invaluable comments. We are very grateful to Secretaría de Marina SEMAR for their continuous support during field operations, in particular, we would like to thank the Dirección de Investigación y Desarrollo, the Oceanographic Station at Salina Cruz, the ASTIMAR 20, and the Decima Zona Naval Militar. We gratefully acknowledge support for this work from CONACYT (project 62520, DirocIOA) and UC-MexUS-CONACYT (collaborative project grant). The INTOA field experiment was supported by CONACYT (SEP-2003-C02-44718). Suggestions and comments from anonymous reviewers enriched this work.

References

Anctil, F., M. A. Donelan, W. M. Drennan, and H. C. Graber (1994), Eddy-correlation measurements of air-sea fluxes from a discus buoy, *J. Atmos. Oceanic Technol.*, *11*, 1144–1150.

Barton, E. D., M. L. Argote, J. Brown, P. M. Kosro, M. F. Lavín, J. M. Robles, R. L. Smith, A. Trasvi na, and H. S. Velez (1993), Supersquirt: Dynamics of the Gulf of Tehuantepec, Mexico, *Oceanography*, *6*(1), 23–30.

Chen, G., and S. E. Belcher (2000), Effects of long waves on wind generated waves, *J. Phys. Oceanogr.*, *30*, 2246–2256.

Donelan, M. A. (1987), The effect of swell on the growth of wind waves, *Johns Hopkins APL Tech. Dig.*, *8*(1), 18–23.

Donelan, M. A. (1990), Air-sea interaction, in *The Sea, vol. 9, Ocean Engineering Science*, edited by B. Le Mehaute and D. M. Hanes, pp. 239–292, Harvard Univ. Press, Cambridge, Mass.

Donelan, M. A., and F. W. Dobson (2001), The influence of swell on the drag, in *Wind Stress Over the Ocean*, edited by I. S. F. Jones and Y. Toba, pp. 181–190, Cambridge Univ. Press, Cambridge, U. K.

Donelan, M. A., J. Hamilton, and W. H. Hui (1985), Directional spectra of wind generated waves, *Philos. Trans. R. Soc. London Ser. A*, *315*, 509–562.

Donelan, M. A., F. W. Dobson, S. D. Smith, and R. J. Anderson (1993), On the dependence of sea surface roughness on wave development, *J. Phys. Oceanogr.*, *23*, 2143–2149.

Donelan, M. A., W. M. Drennan, and K. B. Katsaros (1997), The air-sea momentum flux in conditions of wind sea and swell, *J. Phys. Oceanogr.*, *27*, 2087–2099.

Drennan, W. M. (2006), On parameterisations of air-sea fluxes, in *Atmosphere-Ocean Interactions*, vol. 2, edited by W. Perrie, pp. 1–34, WIT Press, Southampton, U. K.

Drennan, W. M., M. A. Donelan, N. Madsen, K. B. Katsaros, E. A. Terray, and C. N. Flagg (1994), Directional wave spectra from a swath ship at sea, *J. Atmos. Oceanic. Technol.*, *11*, 1109–1116.

Drennan, W. M., K. K. Khama, and M. A. Donelan (1999), On momentum flux and velocity spectra over waves, *Boundary Layer Meteorol.*, *92*, 489–513.

Drennan, W. M., H. C. Graber, D. Hauser, and C. Quentin (2003), On the wave age dependence of wind stress over pure wind seas, *J. Geophys. Res.*, *108*(C3), 8062, doi:10.1029/2000JC000715.

Drennan, W. M., P. K. Taylor, and M. J. Yelland (2005), Parameterizing the sea surface roughness, *J. Phys. Oceanogr.*, *35*, 835–848, doi:10.1175/JPO2704.1.

Geernaert, G. L., F. Hansen, and M. Courtney (1993), Directional attributes of the ocean surface wind stress vector, *J. Geophys. Res.*, *98*(C9), 16,571–16,582.

Godfery, J. S., and A. C. M. Beljaars (1991), On the turbulent fluxes of bouyancy, heat and moisture at the air-sea interface at low wind speeds, *J. Geophys. Res.*, *96*, 22,043–22,048.

Graber, H. C., E. A. Terray, M. A. Donelan, W. M. Drennan, J. C. V. Leer, and D. B. Peters (2000), ASIS—A new Air-Sea Interaction Spar buoy: Design and performance at sea, *J. Atmos. Oceanic. Technol.*, *17*(5), 708–720.

Grachev, A. A., and C. W. Fairall (1997), Dependence of the monin-obukhov stability parameter on the buk richardson number over the ocean, *J. App. Meteorol.*, *36*, 406–415.

Grachev, A. A., C. W. Fairall, J. E. Hare, J. B. Edson, and S. D. Miller (2003), Wind stress vector over ocean waves, *J. Phys. Oceanogr.*, *33*, 2408–2429.

Guo-Larsen, X. V., K. Makin, and A. S. Smedman (2003), Impact of waves on the sea drag: Measurements in tha baltic sea and a model interpretation, *Global Atmos. Ocean Syst.*, *9*, 97–120.

Jones, I. S. F., Y. Volkov, Y. Toba, S. Larsen, and N. E. Huang (2001), Overview, in *Wind Stress Over the Ocean*, edited by I. S. F. Jones and Y. Toba, pp. 1–31, Cambridge Univ. Press, Cambridge, U. K.

Kahma, K. K., and C. J. Calkoen (1996), Growth curve observations, in *Dynamics and Modeling of Ocean Waves*, edited by G. J. Komen et al., pp. 174–182, Cambridge Univ. Press, Cambridge, U. K.

Kudryavstev, V. N., and V. K. Makin (2004), Impact of swell on the marine atmospheric boundary layer, *J. Phys. Oceanogr.*, *34*, 934–949.

Large, W. G., and S. Pond (1981), Open ocean momentum flux mesurements in moderate to strong winds, *J. Phys. Oceanogr.*, *11*, 324–336.

Makin, V. K., H. Branger, W. L. Pierson, and J. P. Giovanangeli (2007), Stress above wind-plus-paddle waves: Modeling of a laboratory experiment, *J. Phys. Oceanogr.*, *37*, 2824–2837, doi:10.1175/2007JPO3550.1.

Masson, D. (1993), On the nonlinear coupling between swell and wind waves, *J. Phys. Oceanogr.*, *23*, 1249–1258.

Miyake, M., R. W. Stewart, and R. W. Burling (1970), Spectra and cospectra of turbulence over water, *Q. J. R. Meteorol. Soc.*, *96*, 138–143.

Monin, A. S., and A. M. Obukhov (1954), Basic laws of turbulent mixing in the ground layer of the atmosphere, *Akad. Nauk. SSSR Geofiz. Inst. Tr.*, *151*, 163–187.

Pan, J., D. W. Wang, and P. A. Hwang (2005), A study of wave effects on wind stress over the ocean in a fetch-limited case, *J. Geophys. Res.*, *110*, C02020, doi:10.1029/2003JC002258.

Phillips, O. M., and M. L. Banner (1974), Wave breaking in the presence of wind drift and swell, *J. Fluid. Mech.*, *66*, 625–640.

Rieder, K. F., J. A. Smith, and R. A. Weller (1994), Observed directional characteristics of the wind, wind stress, and surface waves on the open ocean, *J. Geophys. Res.*, *99*(C11), 22,589–22,596.

Romero, L., and W. K. Melville (2009), Airborne observations of fetch-limited waves in the Gulf of Tehuantepec, *J. Phys. Oceanogr.*, in press.

Smith, S. D. (1980), Wind stress and heat flux over the ocean in gale force winds, *J. Phys. Oceanogr.*, *10*, 709–726.

Smith, S. D. (1988), Coefficeints for sea surface wind stress, heat flux and wind profiles as a function of wind speed and temperature, *J. Geophys. Res.*, *93*, 15,467–15,472.

Smith, S. D. (1989), Water vapor flux at the sea surface, *Boundary Layer Meteorol.*, *10*, 277–293.

Taylor, J. R. (1997), *An Introduction to Error Analysis: The Study of Uncertainties in Physical Measurements*, 327 pp., Univ. Sci. Books, Sausalito, Calif.

Toba, Y., and I. S. F. Jones (2001), The influence of unsteadiness, in *Wind Stress Over the Ocean*, edited by I. S. F. Jones and Y. Toba, pp. 190–205, Cambridge Univ. Press, Cambridge, U. K.

Wright, J. W. (1976), The wind drift and wave breaking, *J. Phys. Oceanogr.*, *6*, 402–405.

Wu, J. (1994), The sea surface is aerodynamically rough even under ligth winds, *Boundary Layer Meteorol.*, *69*, 149–158.

Yelland, M., and P. K. Taylor (1996), Wind stress measurements form the open ocean, *J. Phys. Oceanogr.*, *26*, 541–555.

Young, I. R. (2006), Directional spectra of hurricane wind waves, *J. Geophys. Res.*, *111*, C08020, doi:10.1029/2006JC003540.

M. A. Donelan, Division of Applied Marine Physics, Rosenstiel School of Marine and Atmospheric Science, University of Miami, 4600 Rickenbacker Cswy., Miami, FL 33149-1098, USA.

H. García-Nava, F. J. Ocampo-Torres, and P. Osuna, Departamento de Oceanografía Física, Centro de Investigación Científica y de Educación Superior de Ensenada, Km. 107 Carretera Tijuana-Ensenada, Ensenada, BC 22860, Mexico. (hgarcia@cicese.mx)